Research Square

Preprints are preliminary reports that have not undergone peer review.
They should not be considered conclusive, used to inform clinical practice,
or referenced by the media as validated information.

Air-hole geometry design of ram-extruded polytetrafluoroethylene coaxial cables for low-loss and reproducible operation

Eunsung Jang
Ajou University
Eunsung You
Ajou University
Jeong-Wook Kim
jeongwookkim@ajou.ac.kr

Ajou University

Article

Keywords: Coaxial cable, Polytetrafluoroethylene, Ram extrusion, Air-hole dielectric, Effective permittivity, Dielectric loss

Posted Date: November 24th, 2026

DOI: https://doi.org/10.21203/rs.3.rs-11670118/v1

License: This work is licensed under a Creative Commons Attribution 4.0 International License.
Read Full License

Additional Declarations: No competing interests reported.

Air-hole geometry design of ram-extruded polytetrafluoroethylene coaxial cables for low-loss and reproducible operation

Eunsung Jang[1], Eunsung You[2], Jeong-Wook Kim[3*]

[1]Department of Artificial Intelligence Convergence Network Engineering, Ajou University, Suwon, 16499, Republic of Korea.
[2]Sensorview Co., Ltd., Seongnam, 13449, Republic of Korea.
[3*]Department of Electrical and Computer Engineering, Ajou University, Suwon, 16499, Republic of Korea.

*Corresponding author(s). E-mail(s): jeongwookkim@ajou.ac.kr;
Contributing authors: jangstar@ajou.ac.kr; ssjh0813@naver.com;

Abstract

The loss of coaxial cables rises with frequency as radio-frequency systems move toward tens of gigahertz, and part of this loss comes from the dielectric between the two conductors. Here we lower the effective permittivity of a polytetrafluoroethylene (PTFE) dielectric by forming longitudinal air holes during ram extrusion, and we treat the number, diameter and cross-sectional shape of the holes as design variables under a fixed 50 **Ω** impedance. Full-wave simulation, checked against Maxwell-Garnett effective-medium theory, shows that the holes reduce the dielectric loss in proportion to the air fraction, whereas the conductor loss falls when the dielectric is first perforated and then saturates. A design with six 0.3 mm holes captures this reduction while keeping the loss insensitive to deformation of the holes. Measured from 0 to 18 GHz, the fabricated cable has an effective permittivity of 1.91 and an insertion loss of 1.90 dB/m at 18 GHz with a 2.33 mm outer diameter, lower than two of three commercial cables of larger diameter. In a pilot batch of 600 cables, every cable stayed within 1 **Ω** of 50 **Ω** and the loss differed by less than 0.05 dB/m between batches.

Keywords: Coaxial cable, Polytetrafluoroethylene, Ram extrusion, Air-hole dielectric, Effective permittivity, Dielectric loss

Introduction

Sixth-generation (6G) communication systems are expected to use frequency bands above several tens of gigahertz for high-speed, low-latency and massive-connectivity services [1–7]. At these frequencies the attenuation of transmission lines grows, and reducing the loss of wired media such as coaxial cables becomes a practical requirement [8–10]. The dielectric layer of a coaxial cable sets its impedance, insertion loss and mechanical stability, and low loss at high frequency calls for a dielectric with low permittivity and low loss tangent [11–13]. Polytetrafluoroethylene (PTFE) is widely used for this purpose because of its low permittivity, thermal stability and low moisture absorption [14]. As systems require more compact cables, reducing the cable diameter alone is not sufficient, because tighter field confinement increases both the conductor resistance and the dielectric loss. Compact low-loss cables therefore need structural engineering of the PTFE dielectric rather than geometric scaling.

Introducing air, which has near-unity permittivity and negligible loss, into the dielectric lowers its effective permittivity. Existing methods fall into three groups. Material-based techniques add low-permittivity inclusions such as hollow silica microspheres and reach effective permittivity values near 1.94 above 10 GHz [15, 16]. Structural designs add macroscopic air cavities or perforations for explicit permittivity control [17, 18]. Process-based methods such as foam extrusion generate gas bubbles inside the dielectric [19]. By raising the characteristic impedance and lowering the surface current density, air inclusion also helps reduce the conductor loss [11]. Each route has limits in compact cables. Composites suffer from dispersion and interface losses that degrade wideband performance. Foam extrusion produces randomly distributed pores of varying size, which causes impedance fluctuation along the cable [19]. Dual extrusion and complex structural fabrication add processing time, specialized dies and mechanical weak points [20, 21].

A more controllable alternative is to form air holes that run continuously and uniformly along the cable axis. In PTFE coaxial dielectrics such air regions have been formed in two ways. In the first, the paste-extruded PTFE is drawn faster than the conductor so that stretching forms the air structure [22, 23]; the air content is then governed mainly by the draw ratio rather than by the size or position of individual voids, and the structure tends toward distributed microporosity. In the second, longitudinal cells are shaped directly by dedicated tooling, either as annular-sector cells formed by section members or spacers [24, 25] or as channels formed during paste extrusion [26]. These approaches establish that introducing air lowers the permittivity. The number, diameter and cross-sectional shape of the air holes, however, have not been treated as design variables and related quantitatively to the effective permittivity, insertion loss and characteristic impedance under a fixed 50 Ω constraint, and the repeatability of such a structure in volume production has not been reported.

This work addresses these points. A longitudinally uniform air-hole PTFE dielectric is formed by ram extrusion (Fig. 1), and the hole number, the hole diameter from 0.3 to 0.6 mm and the cross-sectional shape are varied as design variables. The resulting effective permittivity, insertion loss and impedance are quantified by full-wave simulation and cross-checked against the Maxwell-Garnett prediction, with every configuration held to a 50 Ω match. A solid reference and the selected six-hole design are

fabricated and measured from 0 to 18 GHz against three commercial cables (9S40, MWX241 and RG402), and the design is carried into a pilot production of 600 cables.

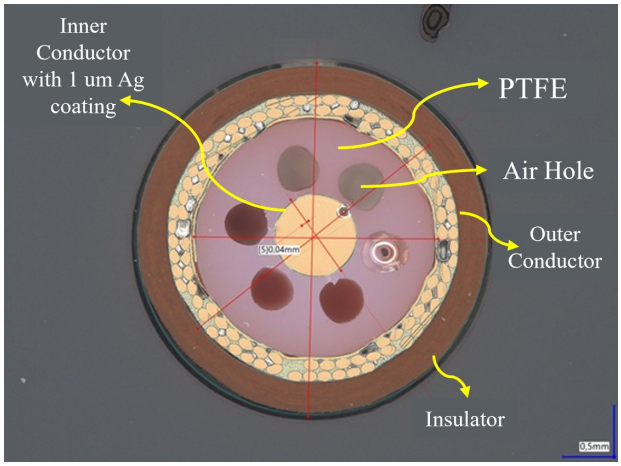


Fig. 1: **Proposed coaxial cable.** Cross-sectional micrograph of the fabricated cable. The inner conductor, coated with a thin conductive film, is surrounded by a ram-extruded PTFE dielectric containing six longitudinal air holes arranged with rotational symmetry, which is enclosed by the outer conductor and an insulating jacket.

Results

Loss model of the air-hole dielectric

Wave propagation along the cable is described by the complex propagation constant $\gamma = \alpha + j\beta$, where α is the attenuation constant and β the phase constant. In a coaxial line filled with a homogeneous low-loss dielectric, the fundamental mode is transverse electromagnetic (TEM). When the dielectric contains longitudinal air holes that are electrically small and arranged with rotational symmetry, the longitudinal field components remain negligible and the mode is well described as quasi-TEM. The attenuation then separates into conductor and dielectric contributions [27, 28],

$$\alpha \approx \alpha_c + \alpha_d. \tag{1}$$

Because the holes are longitudinal cylinders and the field is transverse, the perforated PTFE is represented by the Maxwell-Garnett permittivity for cylindrical inclusions under transverse polarization. For identical circular holes distributed in the PTFE host [29–34],

$$\varepsilon_{\text{eff}} = \varepsilon_h + \frac{2 f_a \, \varepsilon_h \, (\varepsilon_i - \varepsilon_h)}{\varepsilon_i + \varepsilon_h - f_a \, (\varepsilon_i - \varepsilon_h)}, \qquad f_a = \frac{N A_h}{A_{\text{total}}}, \tag{2}$$

where $\varepsilon_h = \varepsilon_r(1 - j\tan\delta)$ is the complex permittivity of PTFE, $\varepsilon_i = 1$ that of air, and f_a the air fraction for N holes of area A_h in a dielectric of cross-sectional area A_{total}. Below, ε_{eff} denotes the real part, and the loss is described by the effective loss tangent $\tan\delta_{\text{eff}}$ (Methods). PTFE is non-polar and its permittivity is essentially constant through the millimetre-wave region [35, 36], so ε_{eff} and $\tan\delta_{\text{eff}}$ are frequency independent for a given geometry.

The dielectric attenuation of a low-loss TEM line is [11]

$$\alpha_d \approx \frac{\pi f}{c}\,\tan\delta_{\text{eff}}\,\sqrt{\varepsilon_{\text{eff}}}, \tag{3}$$

where c is the speed of light. Adding holes lowers both ε_{eff} and $\tan\delta_{\text{eff}}$, so α_d decreases monotonically with the air fraction and scales as f.

The conductor attenuation follows a different balance. At a fixed cross section, a lower ε_{eff} raises the intrinsic impedance of the dielectric, weakens the magnetic field at a given transmitted power and lowers the surface current on the conductors (Methods). The closed-form attenuation constant carries the same dependence [11],

$$\alpha_c = \frac{R_s\sqrt{\varepsilon_{\text{eff}}}}{2\eta_0\,\ln(b/a)}\left(\frac{1}{a}+\frac{1}{b}\right), \tag{4}$$

where a and b are the inner and outer conductor radii, $R_s = \sqrt{\pi f\mu_0/\sigma}$ is the surface resistance and η_0 the free-space impedance. This expression cannot be read with ε_{eff} varied alone, because the design must remain matched to 50 Ω. The characteristic impedance

$$Z_0 = \frac{\eta_0}{2\pi\sqrt{\varepsilon_{\text{eff}}}}\,\ln(b/a) \tag{5}$$

couples ε_{eff} to the geometry, and with the inner radius a fixed, holding Z_0 at 50 Ω forces b to shrink as ε_{eff} is lowered. Substituting the match condition into equation (4) gives

$$\alpha_c = \frac{R_s}{4\pi Z_0}\left(\frac{1}{a}+\frac{1}{b}\right), \tag{6}$$

in which the $\sqrt{\varepsilon_{\text{eff}}}$ factor cancels: the field-level reduction is offset by the smaller b needed to restore the match. With a fixed, the term $1/a$ dominates, so the conductor loss depends only weakly on the number of holes once the match is imposed. The reduction from the field redistribution is largest when the dielectric is first perforated; as more holes are added it is progressively offset by the shrinking b, and the conductor loss saturates. The dielectric loss, by contrast, keeps decreasing with the air fraction, so the number and size of the holes must be chosen rather than increased without limit.

Single-mode operation requires the band to lie below the cutoff of the first higher-order mode, TE_{11}, [11]

$$f_c \approx \frac{c}{\pi(a+b)\sqrt{\varepsilon_{\text{eff}}}}. \tag{7}$$

The lower ε_{eff} and the smaller b required for the match both raise f_c.

Field structure, matching and single-mode band

Full-wave simulations were carried out with the inner conductor radius fixed at $a = 0.4$ mm and the outer radius b adjusted for 50 Ω in every configuration, so that the air-hole structure is the only design variable (Methods; Supplementary Table 2; Supplementary Table 3). Figure 2a shows the model with 50 Ω connectors, and Fig. 2b–f show the cross-sectional electric field of the six-hole design with $d_1 = 0.3$ mm from 2 to 18 GHz. At every frequency the field is directed radially from the inner to the outer conductor with no axial component, the pattern expected for the dominant TEM mode of a coaxial line, so the perforated dielectric lowers the effective permittivity without altering the fundamental field structure. The reflection coefficient in Fig. 3a was obtained from this connector-integrated model and therefore includes the impedance transition at the connector interface; it confirms that the design remains matched to 50 Ω under realistic launch conditions.

Figure 3b compares the TE_{11} cutoff from equation (7) with the simulated values. The lowest cutoff exceeds 39 GHz for every configuration and increases with the number of holes, with calculated and simulated curves agreeing closely. Because this cutoff lies well above 18 GHz, only the quasi-TEM mode propagates over the band of interest.

Loss decomposition versus the number of holes

The effective permittivity in Fig. 4a decreases monotonically with the number of holes, from about 2.10 for the solid-PTFE reference to 2.02, 1.94, 1.86 and 1.78 for the 3-, 6-, 9- and 12-hole designs. For each configuration the value obtained from the solver and the value extracted from the simulated S_{21} phase (Methods) agree closely and remain nearly constant across the band. The effective loss tangent in Fig. 4b follows the same order, from about 2.0×10^{-4} for the reference to 1.55×10^{-4} for the 12-hole design. Its weak frequency variation comes from the causal dispersion model used to represent the PTFE loss in the solver and not from a dispersion of PTFE itself (Methods). The two reductions combine in the dielectric loss of Fig. 4c, which rises with frequency as equation (3) predicts and at 18 GHz falls from about 0.66 dB/m for the reference to 0.52, 0.48, 0.42 and 0.36 dB/m for the 3-, 6-, 9- and 12-hole designs.

The surface current density in Fig. 4d drops when the solid dielectric is first perforated and then changes little. At 9 GHz it falls from about 46.4 A/m for the reference to 45.6 A/m for three holes, and then by less than 0.1 A/m per step to 45.5, 45.4 and 45.4 A/m for six, nine and twelve holes. The conductor loss in Fig. 4e follows the same trend: the reference is highest at about 2.37 dB/m at 18 GHz, whereas the four air-hole designs lie close together at 2.04, 2.00, 1.93 and 1.88 dB/m. This is the behaviour expected from equation (6): the field redistribution reduces the conductor loss at the first perforation, after which the match condition leaves the loss set mainly by the conductor geometry.

The total insertion loss in Fig. 4f combines both contributions. The reference reaches about 3.0 dB/m at 18 GHz, while the air-hole designs lie between roughly 2.2 and 2.6 dB/m. Because the conductor loss dominates over most of the band, its saturation carries over to the insertion loss, with the largest improvement between the reference and the first air-hole design and small differences among the 3-, 6-, 9- and 12-hole cases.

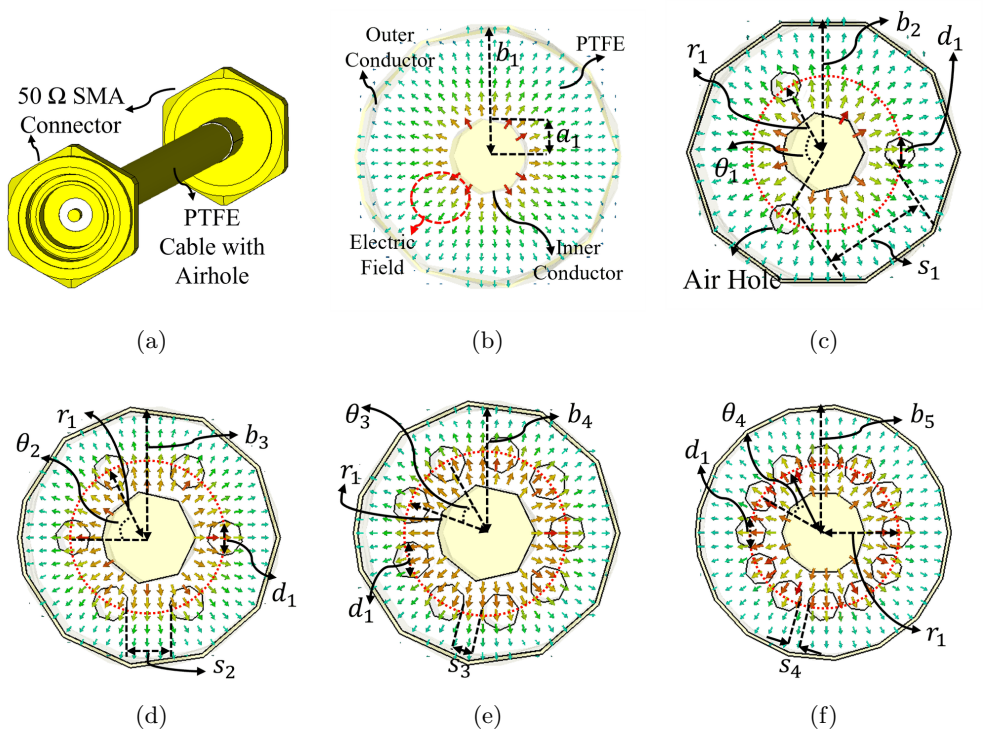


Fig. 2: **Simulated model and quasi-TEM field of the six-hole design** ($d_1 =$ 0.3 **mm). a**, Full model with connectors. **b–f**, Cross-sectional electric field at 2, 4, 8, 12 and 18 GHz, directed radially from the inner to the outer conductor; the radial pattern is preserved across the band.

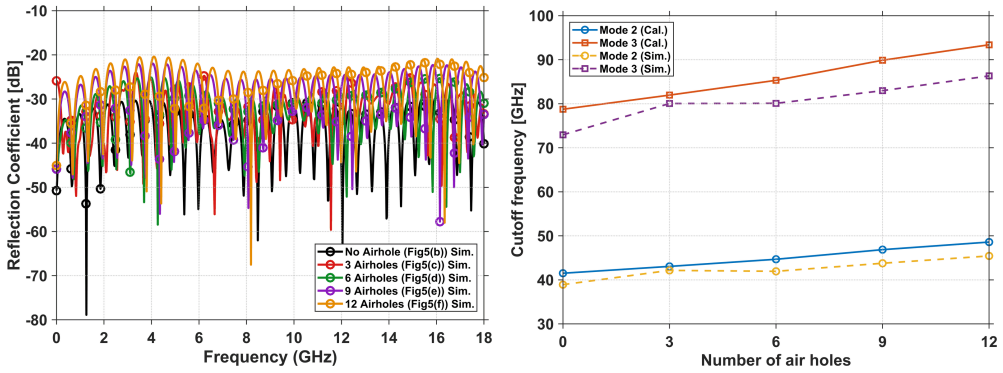


Fig. 3: **Simulated matching and single-mode band. a**, Reflection coefficient from the connector-integrated full-wave model. **b**, Cutoff frequency of the first higher-order mode (TE_{11}) for each cross section, calculated from equation (7) and simulated.

This saturation has a design consequence. Adding holes beyond a few gives little further loss reduction but thins the dielectric webs between holes, from $s_1 = 1.15$ mm for three holes to $s_2 = 0.49$ mm for six and $s_3 = 0.23$ mm for nine (Supplementary Table 3). Thinner webs are more easily distorted when the cable is bent, and distortion changes the local air fraction and therefore the effective permittivity. The configuration therefore cannot be chosen by loss minimization alone; the sensitivity of the loss to deformation must be included.

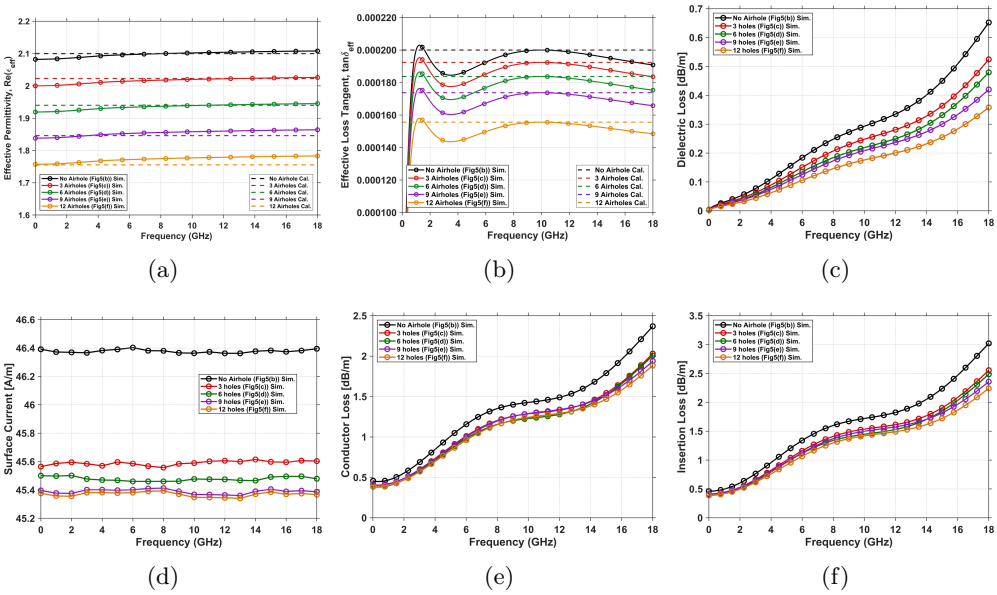


Fig. 4: **Simulated effective-medium parameters and loss components for the $d_1 = 0.3$ mm series. a**, Effective permittivity from the solver and from the simulated S_{21} phase, compared with the Maxwell-Garnett calculation. **b**, Effective loss tangent. **c**, Dielectric loss. **d**, Surface current density. **e**, Conductor loss. **f**, Total insertion loss. Each panel compares the solid reference with the 3-, 6-, 9- and 12-hole designs.

Choice of hole number and diameter under deformation

In service the cable is bent and flexed, which applies transverse pressure to the dielectric and can distort the circular holes. To assess this, each circular hole of radius r was deformed into an ellipse with major axis $A = r/k$ and minor axis $B = kr$, so that $\pi AB = \pi r^2$ and the air fraction is unchanged while only the shape varies (Fig. 5a–h). Deformation factors $k_1 = 0.9$ and $k_2 = 0.8$ were compared with the circular case $k = 1.0$. Because the insertion loss saturates once a few holes are added while its variation under distortion does not, the configuration was selected by how little the loss moves under deformation.

The hole diameter was fixed first. Comparing the $d_1 = 0.3$ mm series in Fig. 5i with the larger-diameter series in Fig. 5j, the 0.3 mm series fluctuates far less at every hole count: at 18 GHz its loss varies by a few percent of the nominal value, whereas the larger holes vary roughly three to six times more under the same distortion. For the six-hole design, the spread is 2.5% of the nominal loss at 0.3 mm but 9.2% for the larger holes. Enlarging the holes lowers the nominal loss only marginally once the loss has saturated, but multiplies the deformation sensitivity, so the 0.3 mm diameter was adopted. Within this series, the 18 GHz spread grows from 1.2% at three holes to 2.5% at six, 4.1% at nine and 15.0% at twelve. Adding holes beyond six barely lowers the saturated loss but amplifies its sensitivity to distortion, with the twelve-hole loss varying about six times as much as the six-hole loss. The six-hole design sits at the onset of saturation, capturing the loss reduction of the air-hole structure while its variation under distortion is still small, and the six-hole, $d_1 = 0.3$ mm configuration was selected.

Measured performance

A solid PTFE reference without holes and the six-hole design with $D = 0.3$ mm were fabricated and measured from 0 to 18 GHz together with three commercial cables, 9S40 (Sensorview), MWX241 (Junkosha) and RG402 (RF corea), under identical conditions (Fig. 6a; Methods). The cross-sectional micrograph in Fig. 6a confirms six circular holes of 0.3 mm as designed.

All five cables keep the reflection coefficient below about −15 dB across the band (Fig. 6b). At low and middle frequencies the reference and the six-hole cable behave similarly and stay below −20 dB, so the holes do not degrade the impedance of the line. Above 14 GHz both fabricated cables rise to about −15 to −20 dB, whereas the commercial cables flatten or fall slightly. Because the reference, which has no holes, rises in the same way, this difference comes from the hand-assembled connector transitions of the two prototypes and not from the air-hole dielectric.

The effective permittivity extracted from the measured S_{21} phase (Fig. 6c) is about 2.10 for the reference, matching bulk PTFE, and about 1.91 for the six-hole cable, both nearly constant across the band. The six-hole value differs from the simulated 1.94 by about 0.03, within roughly 1.5%, so the effective-medium model and the full-wave simulation predict the permittivity of the fabricated cable. The commercial cables range from about 1.61 for 9S40, indicating a highly porous dielectric, to 2.09 and 2.11 for MWX241 and RG402, consistent with near-solid PTFE.

The insertion loss of all cables rises with frequency (Fig. 6d), and the six-hole cable stays below the solid reference across the band. Table 1 lists the values. At 18 GHz the six-hole cable reaches 1.90 dB/m, lower than MWX241 (2.18 dB/m) and RG402 (2.02 dB/m) although its outer diameter of 2.33 mm is the smallest of the five, and 10.4% lower than the reference (2.12 dB/m), which has the same conductor geometry. At 12 GHz it reaches 1.48 dB/m.

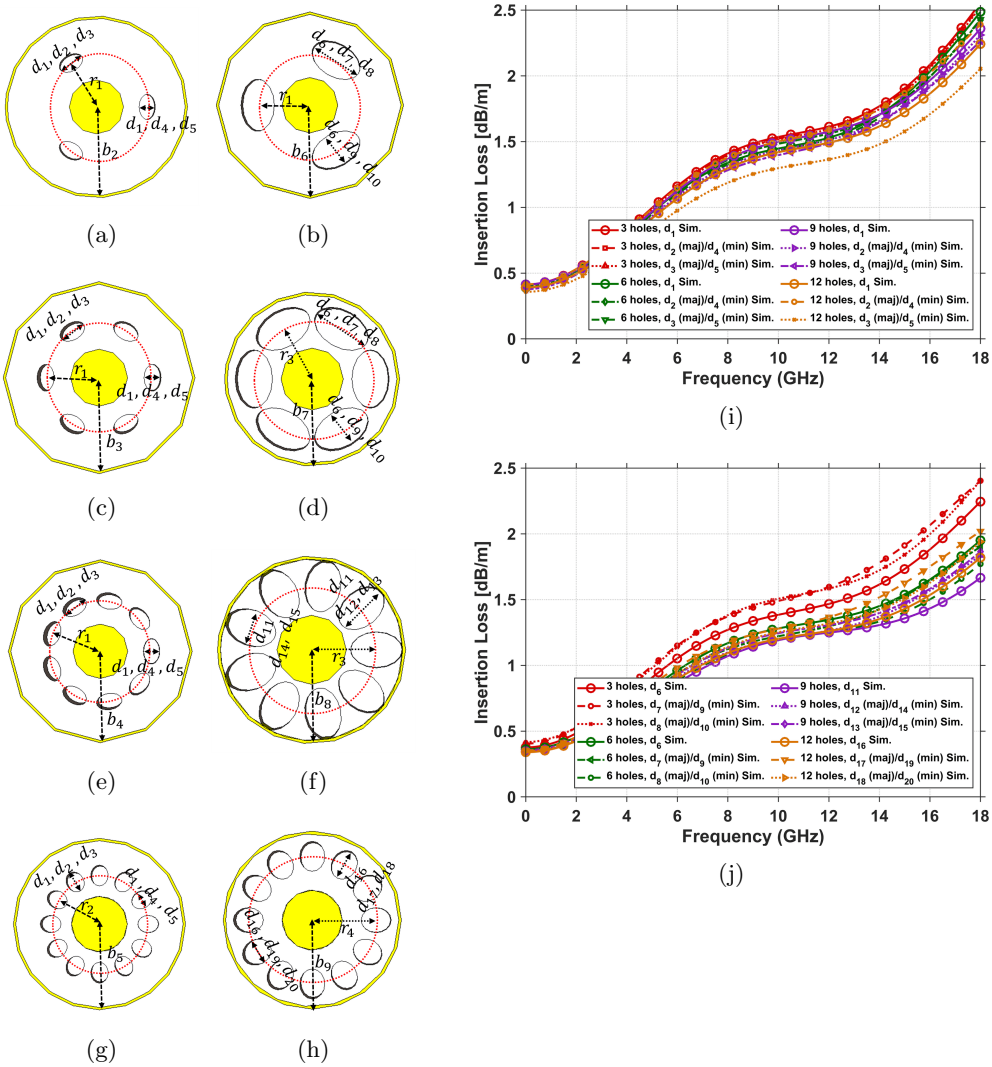


Fig. 5: **Sensitivity of the insertion loss to hole deformation. a–h**, Simulated cross sections comparing the nominal holes with the major-axis (d/k) and minor-axis ($d \cdot k$) cases for $k_1 = 0.9$ and $k_2 = 0.8$. Left column, $d_1 = 0.3$ mm series; right column, larger-diameter series: **a**,**b** three holes; **c**,**d** six holes; **e**,**f** nine holes; **g**,**h** twelve holes, with $d_6 = 0.6$ mm for three and six holes, $d_{11} = 0.5$ mm for nine holes and $d_{16} = 0.4$ mm for twelve holes. **i**,**j**, Simulated insertion loss of the nominal ($d/k = 1$) and deformed cross sections for the $d_1 = 0.3$ mm series (**i**) and the larger-diameter (0.4, 0.5 and 0.6 mm) series (**j**).

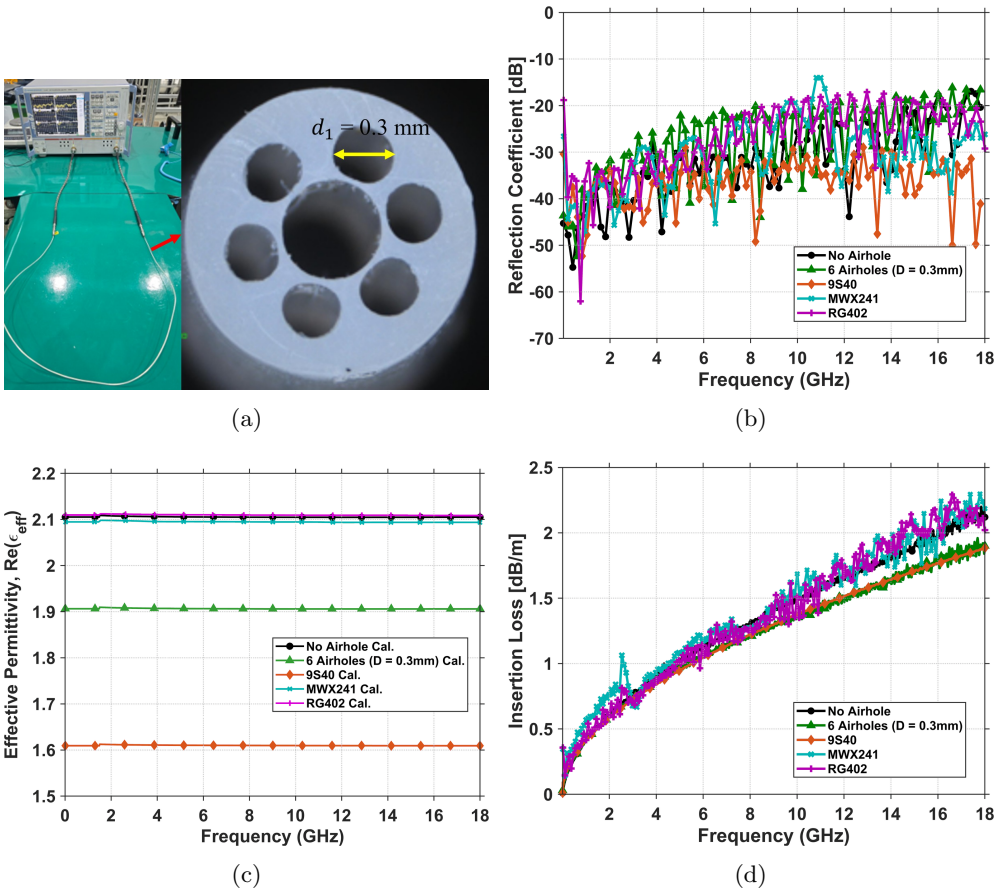


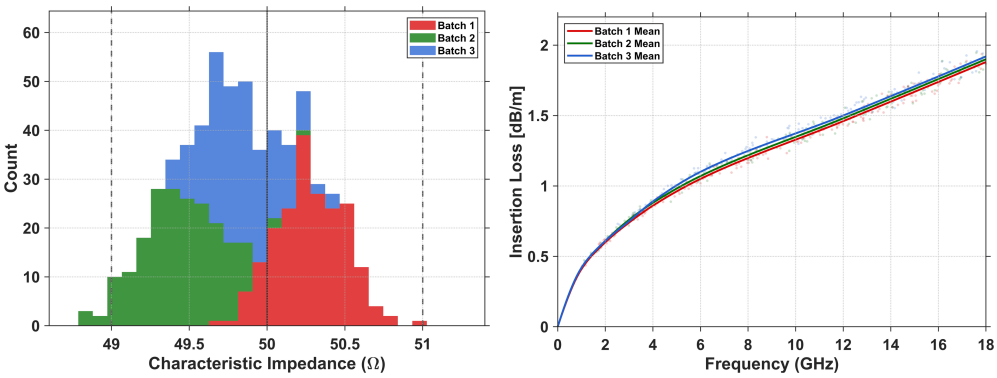
Fig. 6: **Measured performance of the fabricated and commercial cables. a**, Measurement setup with the fabricated cable (red arrow) and a cross-sectional micrograph of the six-hole PTFE dielectric ($d_1 = 0.3$ mm, inset). **b**, Reflection coefficient S_{11}. **c**, Effective permittivity extracted from the measured S_{21} phase. **d**, Insertion loss.

Repeatability in pilot production

A pilot batch of 600 cables was produced by the same ram extrusion process in three runs of 200 m each (batches 1–3). The measured characteristic impedance of all 600 cables clusters around 50 Ω and every cable falls within ±1 Ω (Fig. 7a), tighter than the ±2 Ω tolerance specified for comparable semi-rigid cables in MIL-DTL-17 [37]. The batch means were 50.28, 49.44 and 49.83 Ω. The insertion loss shows the same consistency (Fig. 7b): the per-batch mean curves are nearly indistinguishable, and the largest batch-to-batch difference is below 0.05 dB/m over 1–18 GHz.

Table 1: Measured insertion loss of the commercial cables, the solid reference and the proposed cable. OD is the outer diameter including the dielectric layer, and ε_{eff} was extracted from the measured S_{21} phase. Values of $\tan\delta$ are manufacturers' datasheet values for the three commercial cables and simulation-based values for the reference and proposed cables. The proposed cable has six air holes with $D = 0.3$ mm.

	OD				Insertion loss (dB/m)				
Cable	(mm)	Dielectric	ε_{eff}	$\tan\delta$	1	3	6	12	18 GHz
9S40	2.67	Aeroflon	1.61	0.0001	0.41	0.73	1.04	1.52	1.88
MWX241	4.10	PTFE	2.09	0.0002	0.57	0.75	1.17	1.71	2.18
RG402	2.95	PTFE	2.11	0.0002	0.42	0.74	1.10	1.72	2.02
Reference	2.46	PTFE	2.10	0.0002	0.41	0.76	1.13	1.65	2.12
Proposed	2.33	Air + PTFE	**1.91**	0.00018	**0.41**	**0.73**	**1.05**	**1.48**	**1.90**



(a) (b)

Fig. 7: **Uniformity over 600 cables from three production batches. a**, Distribution of the measured characteristic impedance relative to the $50 \pm 1\ \Omega$ band. **b**, Insertion loss versus frequency with the per-batch mean curves overlaid.

Discussion

The comparison in Table 1 shows where the improvement comes from. The four PTFE-based cables, MWX241, RG402, the solid reference and the proposed cable, all have loss tangents close to 2×10^{-4}, with the proposed cable marginally lower at 1.8×10^{-4}, so their differences in insertion loss come mainly from the effective permittivity and the cross-sectional dimensions rather than from the intrinsic material loss. The air holes act directly on ε_{eff} and lower the dielectric attenuation, while the conductor attenuation drops from the solid reference to the first air-hole design and then saturates under the 50 Ω match. Because the solid reference, RG402 and the proposed cable share nearly the same conductor geometry and therefore sit in this saturated regime,

the lower insertion loss of the proposed cable among the PTFE cables comes mainly from its lower effective permittivity, 1.91 against 2.09 to 2.11, without any change of base material.

The proposed cable also approaches 9S40 (1.88 dB/m), which uses Aeroflon with an effective permittivity of 1.61 and a loss tangent of 1×10^{-4}. Starting from a material with twice the loss tangent and a higher permittivity, the air-hole structure narrows the difference to 0.02 dB/m through geometry. Unlike a fixed-property material, the air-hole dielectric allows $\varepsilon_{\mathrm{eff}}$ to be set by the hole count and diameter; the simulations covered values from about 2.10 to 1.78 within the same base material and process. Because the measured permittivity of the six-hole cable agrees with the simulated and calculated values within about 1.5%, this adjustment can be made by design.

The pilot batch shows that these properties carry over to production. Every one of 600 cables stayed within $\pm 1\ \Omega$ of 50 Ω, and the insertion loss varied by less than 0.05 dB/m between batches. This consistency indicates that the longitudinally uniform holes formed by ram extrusion avoid the impedance fluctuation associated with the random porosity of foam extrusion [19].

Several aspects remain open. The measurements cover 0 to 18 GHz, and measurements above 18 GHz are needed to confirm the behaviour in the millimetre-wave bands targeted by 6G systems. The holes studied here were circular, with diameters of 0.3 to 0.6 mm, or elliptical, all on a single ring at the same radius; other shapes, staggered radii and multiple concentric rings were not examined and may give further control over the effective permittivity and field distribution. Performance after thermal cycling and humidity exposure has not been characterized, and the present batch covers 200 m runs, so scalability to continuous lengths of several kilometres and formal statistical process control remain to be verified.

Methods

Fabrication of the air-hole PTFE dielectric

PTFE cannot be melt-processed by conventional thermoplastic extrusion because of its high viscosity and non-melt-flow behaviour, so PTFE coaxial dielectrics are formed by ram or dual extrusion. The dielectric in this work was formed by ram extrusion in four stages. PTFE powder was first blended for homogeneity. The blended powder was compressed in a preforming mould under controlled temperature and pressure to form a rod, removing trapped air and increasing density. The preform was then forced through a die in a ram extruder under high pressure to obtain the cross section with longitudinal air holes, and the extrudate was sintered at approximately 330 °C to give the dielectric its mechanical strength and electrical stability. Because the extrusion proceeds by solid-state compaction rather than melt flow, the process gives longitudinally continuous holes with dimensional control and reproducibility. A comparison with foam extrusion [19, 38] and dual extrusion [20] is given in Supplementary Note 1, Supplementary Figs. 1–3 and Supplementary Table 1.

Full-wave simulation

The analysis used a three-dimensional time-domain solver based on the finite-integration technique, which discretizes Maxwell's equations in integral form and on a Cartesian grid reduces to a finite-difference time-domain scheme suited to broadband analysis [39]. A single broadband excitation gives the full S-parameter response over 0–18 GHz, and the curved boundaries of the cylindrical air channels are resolved on a hexahedral grid by the perfect-boundary approximation [40]. The same solution provides the cross-sectional electric field and surface current. The inner conductor radius was held at $a = 0.4$ mm and only the air-hole geometry and the outer PTFE radius b were varied, with b set for 50 Ω. Copper conductors (5.8×10^7 S/m) and PTFE with $\varepsilon_r = 2.1$ and $\tan\delta = 0.0002$ at 10 GHz were used. The mesh density was at least 15 cells per wavelength and the transient field was driven to a −40 dB energy-decay level. The settings are listed in Supplementary Table 2 and the geometric parameters of all configurations in Supplementary Table 3.

Effective loss tangent and causal material model

Because the host permittivity in equation (2) is complex, $\varepsilon_{\mathrm{eff}} = \varepsilon'_{\mathrm{eff}} - j\varepsilon''_{\mathrm{eff}}$, and the effective loss tangent is

$$\tan\delta_{\mathrm{eff}} = \varepsilon''_{\mathrm{eff}}/\varepsilon'_{\mathrm{eff}}. \tag{8}$$

For an ideal constant-$\tan\delta$ material, $\varepsilon_{\mathrm{eff}}$ and $\tan\delta_{\mathrm{eff}}$ are frequency independent. In the full-wave solver a strictly constant loss tangent cannot be assigned because it would violate causality, so the PTFE loss was represented by a causal dispersion model of order $N = 3$ that approximates a nearly constant $\tan\delta$ over the band while satisfying the Kramers-Kronig relations [41]. The simulated $\tan\delta_{\mathrm{eff}}$ therefore shows a weak frequency variation, largest near the band edges, which originates from the material model.

Conductor-loss mechanism

A lower $\varepsilon_{\mathrm{eff}}$ raises the intrinsic impedance of the dielectric, $\eta = \sqrt{\mu_0/(\varepsilon_0\varepsilon_{\mathrm{eff}})}$, which sets the ratio of the electric to the magnetic field of the TEM wave, $|\mathbf{E}| = \eta|\mathbf{H}|$. The transmitted power

$$P = \frac{1}{2}\oint \mathrm{Re}\,(\mathbf{E}\times\mathbf{H}^*)\cdot d\mathbf{S} = \frac{\eta}{2}\oint |\mathbf{H}|^2 dS \tag{9}$$

gives, at a fixed power, $|\mathbf{H}| \propto \eta^{-1/2} \propto \varepsilon_{\mathrm{eff}}^{1/4}$. Through $\mathbf{J}_s = \hat{n}\times\mathbf{H}$ the surface current density falls, and so does the conductor power loss per unit length,

$$P_c = \frac{R_s}{2}\oint_C |\mathbf{J}_s|^2 dl, \tag{10}$$

giving $P_c \propto \sqrt{\varepsilon_{\mathrm{eff}}}$ at a fixed geometry. Because the dielectric is nonmagnetic, the distributed inductance is unchanged and $\varepsilon_{\mathrm{eff}}$ enters only through the distributed capacitance $C = 2\pi\varepsilon_0\varepsilon_{\mathrm{eff}}/\ln(b/a)$, which leads to equation (5).

Effective permittivity from the S_{21} phase

The phase of S_{21} carries the phase constant of the cable [42–44]. A wave travelling along a cable of length L accumulates a phase $\phi = -\beta L$ with $\beta = (\omega/c)\sqrt{\varepsilon_{\mathrm{eff}}}$, so from the unwrapped phase

$$\varepsilon_{\mathrm{eff}}(f) = \left[\frac{c\,|\phi(f)|}{2\pi f L}\right]^2 . \tag{11}$$

Because the cables are low loss, the attenuation constant is much smaller than β and the phase alone determines the real part of $\varepsilon_{\mathrm{eff}}$. The same equation was applied to the simulated and measured S_{21}.

Measurements

S-parameters were measured with a vector network analyzer (ZVA40, Rohde & Schwarz) from 0 to 18 GHz. A full two-port short-open-load-thru calibration with an 85052D calibration kit placed the reference plane at the connector interface of the cable under test, so that the test cables and their phase delay lie outside the reference plane. Identical test cables and connectors were used throughout, and the measured S-parameters represent the connector-to-connector response of each cable. Each measured cable was 1 m long, which is the length L in equation (11). The two fabricated cables were assembled with connectors by hand.

Pilot production test

The pilot batch of 600 cables was produced in three runs of 200 m each by the same ram extrusion process. The characteristic impedance of each cable and its insertion loss from 1 to 18 GHz were measured.

Data availability. The data that support the findings of this study are available from Ajou University, but restrictions apply to the availability of these data, which were used with the permission of Ajou University for the current study, and so are not publicly available. The data are, however, available from the corresponding author upon reasonable request and with the permission of Ajou University.

Funding. This work was supported in part by the National Research Foundation of Korea (NRF) grant funded by the Korea government (MSIT) under Grant RS-2025-02303435, and in part by the National Research Foundation of Korea (NRF) grant funded by the Korea government (MSIT) under Grant RS-2025-24535709.

Author contributions. E.J. and E.Y. contributed equally. E.J.: conceptualization, methodology, software, formal analysis, investigation, validation and writing of the original draft. E.Y.: conceptualization, methodology, resources, formal analysis, investigation, validation and writing of the original draft. J.-W.K.: supervision, project administration, funding acquisition and review and editing of the manuscript. All authors reviewed the manuscript.

Competing interests. The authors declare no competing interests.

Supplementary information. Supplementary Note 1, Supplementary Figs. 1–3 and Supplementary Tables 1–3 are provided in a separate file.

References

[1] Zhang, Z. *et al.* 6G wireless networks: Vision, requirements, architecture, and key technologies. *IEEE Veh. Technol. Mag.* **14**, 28–41 (2019).

[2] Lu, Y. & Zheng, X. 6G: A survey on technologies, scenarios, challenges, and the related issues. *J. Ind. Inf. Integr.* **19**, 100158 (2020).

[3] Viswanathan, H. & Mogensen, P. E. Communications in the 6G era. *IEEE Access* **8**, 57063–57074 (2020).

[4] Tataria, H. *et al.* 6G wireless systems: Vision, requirements, challenges, insights, and opportunities. *Proc. IEEE* **109**, 1166–1199 (2021).

[5] Jiang, W. *et al.* Terahertz communications and sensing for 6G and beyond: A comprehensive review. *IEEE Commun. Surveys Tuts.* **26**, 2326–2381 (2024).

[6] Chen, H. *et al.* A tutorial on terahertz-band localization for 6G communication systems. *IEEE Commun. Surveys Tuts.* **24**, 1780–1815 (2022).

[7] Chaccour, C. *et al.* Seven defining features of terahertz (THz) wireless systems: A fellowship of communication and sensing. *IEEE Commun. Surveys Tuts.* **24**, 967–993 (2022).

[8] Wei, Z. *et al.* Integrated sensing and communication signals toward 5G-A and 6G: A survey. *IEEE Internet Things J.* **10**, 11068–11092 (2023).

[9] Mechaik, M. M. *Signal attenuation in transmission lines.* in Proc. IEEE 2nd Int. Symp. Quality Electron. Des. (ISQED), 191–196 (San Jose, CA, USA, 2001).

[10] Miller, C. M. & Sacks, R. C. Dielectric loss in coaxial cables via phase delay measurements. *IEEE Trans. Instrum. Meas.* **IM-23**, 447–454 (1974).

[11] Pozar, D. M. *Microwave Engineering: Theory and Techniques* (Wiley, Hoboken, NJ, USA, 2021).

[12] Lee, S. J. & Yang, H. S. Recent progress and design of three-phase coaxial HTS power cable in Korea. *IEEE Trans. Appl. Supercond.* **29**, 5401505 (2019).

[13] Engelbrecht, J., Collmann, R., Birkel, U. & Weber, M. *Suppression of power level fluctuations at leaky coaxial cable ends using ferrite cores.* in Proc. German Microw. Conf. (GeMiC), 1–4 (Darmstadt, Germany, 2011).

[14] He, X., Yu, C., Liang, Z., Xiao, M. & Li, E. Dielectric and structural properties evolution of PTFE-based high-frequency circuit substrates for mmWave

application under hygrothermal aging. *Polym. Degradation Stability* **234**, 111192 (2025).

[15] Li, Y. *et al.* Ultra-low permittivity HSM/PTFE composites for high-frequency microwave circuit application. *J. Mater. Sci., Mater. Electron.* **33**, 10096–10103 (2022).

[16] Wang, Y., Yang, Z., Wang, H., Li, E. & Yuan, Y. Investigation of PTFE-based ultra-low dielectric constant composite substrates with hollow silica ceramics. *J. Mater. Sci., Mater. Electron.* **33**, 4550–4558 (2022).

[17] Shao, Y. & Zhang, M. A design methodology for low-loss interconnects featuring air cavities and periodically nonuniform widths. *Appl. Sci.* **15**, 2799 (2025).

[18] Mrnka, M. & Raida, Z. An effective permittivity tensor of cylindrically perforated dielectrics. *IEEE Antennas Wireless Propag. Lett.* **17**, 66–69 (2018).

[19] Lee, K. H. & Baek, C. H. Low-loss coaxial cable (2012). Republic of Korea Patent 10-1141064.

[20] Ishii, T., Matsuno, S., Watanabe, K. & Tanaka, S. Thin-diameter coaxial cable and method of producing the same (2005). U.S. Patent Appl. 2005/0230145 A1.

[21] Van Swearingen, K. Coaxial RF device thermally conductive polymer insulator and method of manufacture (2010). U.S. Patent 7 705 238 B2.

[22] Harlow, N. R. Manufacture of low density sintered polytetrafluoroethylene insulated cable (1985). U.S. Patent 4 529 564.

[23] Seo, G.-N. Apparatus for manufacturing dielectric of coaxial cable (2007). Republic of Korea Patent 10-0768799.

[24] Perez, S. Coaxial cable of low dielectric constant, and a fabrication method and tool therefor (2011). U.S. Patent 8 007 700 B2.

[25] Perez, S. & Yeung, C. K. Electric wire having a PTFE covering that is robust and that has a low dielectric constant, and a method and a tool for manufacturing the same (2013). U.S. Patent 8 618 417 B2.

[26] Levy, D. L. & Aeschbach, K. Paste extruded insulator with air channels (2010). U.S. Patent 7 740 781 B2.

[27] Collin, R. E. *Foundations for Microwave Engineering* 2nd edn (Wiley–IEEE Press, Hoboken, NJ, USA, 2007).

[28] Ramo, S., Whinnery, J. R. & Van Duzer, T. *Fields and Waves in Communication Electronics* 3rd edn (Wiley, New York, NY, USA, 1994).

[29] Maxwell Garnett, J. C. XII. Colours in metal glasses and in metallic films. *Philos. Trans. Roy. Soc. London A* **203**, 385–420 (1904).

[30] Brandt, J., Fei, T., Schmitt, S. M., Dreisow, F. & Schmidt, M. A. On the applicability of the Maxwell Garnett effective medium model to media with a high density of cylindrical pores. *Opt. Mater. Express* **14**, 871–879 (2024).

[31] Nisanci, M. H., de Paulis, F., Orlandi, A. & Di Febo, D. From Maxwell Garnett to Debye model for electromagnetic simulation of composite dielectrics—Part II: Random cylindrical inclusions. *IEEE Trans. Electromagn. Compat.* **54**, 280–289 (2012).

[32] Sihvola, A. *Electromagnetic Mixing Formulas and Applications* IEE Electromagnetic Waves Series 47 (Institution of Engineering and Technology, London, U.K., 1999).

[33] Xu, X., Qing, A., Gan, Y. B. & Feng, Y. P. Effective properties of fiber composite materials. *J. Electromagn. Waves Appl.* **18**, 649–662 (2004).

[34] Sihvola, A. H. & Kong, J. A. Effective permittivity of dielectric mixtures. *IEEE Trans. Geosci. Remote Sens.* **26**, 420–429 (1988).

[35] Givot, B., Krupka, J., Lees, K. A., Clarke, R. N. & Hill, G. *Accurate measurements of permittivity and dielectric loss tangent of low loss dielectrics at frequency range 100 MHz–20 GHz.* in Proc. Int. Conf. Microw., Radar Wireless Commun. (MIKON), 232–235 (Krakow, Poland, 2006).

[36] Krupka, J., Salski, B., Kopyt, P. & Cwikla, A. Measurements of the complex permittivity of low loss polymers at frequency range from 5 GHz to 50 GHz. *IEEE Microw. Wireless Compon. Lett.* **26**, 464–466 (2016).

[37] Cables, radio frequency, flexible and semirigid, general specification for. Standard MIL-DTL-17J, Amendment 5, U.S. Dept. Defense (2025).

[38] Jeon, B. J., Cha, S. W. & Lee, K. S. *A study on the foaming characteristics of the insulator for the coaxial cable.* in Proc. Korean Soc. Mech. Eng. (KSME) Conf. (Seoul, Republic of Korea, 2010).

[39] Weiland, T. *RF & microwave simulators—from component to system design.* in Proc. 33rd Eur. Microw. Conf. (EuMC), 591–596 (Munich, Germany, 2003).

[40] Krietenstein, B., Schuhmann, R., Thoma, P. & Weiland, T. *The perfect boundary approximation technique facing the big challenge of high precision field computation.* in Proc. 19th Int. Linear Accel. Conf. (LINAC), 860–862 (Chicago, IL, USA, 1998).

[41] Engin, A. E. Extraction of dielectric constant and loss tangent using new rapid plane solver and analytical Debye modeling for printed circuit boards. *IEEE Trans. Microw. Theory Techn.* **58**, 211–219 (2010).

[42] Cai, L., Jiang, Z. H. & Hong, W. Broadband measurement of substrate complex permittivity using optimized ABCD matrix. *IEEE Access* **8**, 224513–224521 (2020).

[43] Stanley, M. *et al.* Determination of the permittivity of transmission lines at milli-kelvin temperatures. *IEEE Access* **11**, 60626–60634 (2023).

[44] Zhu, H. *et al.* Permittivity measurement of the substrate by using the corrected differential phase method and quick-press test fixture. *Rev. Sci. Instrum.* **93**, 094709 (2022).

Supplementary Files

This is a list of supplementary files associated with this preprint. Click to download.

- SciRepCoaxialCableSI.pdf